

A MULTIPHASE FLUID-SOLID MODEL BASED ON THE LEVEL SET METHOD

James E. HILTON^{1*}

¹ CSIRO Mathematics, Informatics and Statistics, Clayton, Victoria 3169, AUSTRALIA

ABSTRACT

The level set method provides a natural framework for modelling multiphase phenomena in a Eulerian basis. The method is based on the evolution of the signed distance function from interfaces between phases of the flow, and automatically captures complex topological changes of the free surfaces such as breaking and merging. We present an extension to the level set method for modelling the interaction between fluids and elastic solids, where the level set defines the boundary between fluid and solid. The multiphase method varies the underlying stress tensor depending on the sign of the level set, changing smoothly from a rate of strain dependency within the liquid to a hypo-elastic strain dependency within the solid. We apply the model to two test problems, showing the potential of the model for industrial applications involving the coupled interaction of deformable elastic solids and fluids.

NOMENCLATURE

D	rate of strain tensor
E	Young's modulus
\mathbf{f}	body forces
H	Heaviside step function
p	pressure
S_2	2 nd invariant of the strain rate tensor
t	time
\mathbf{v}	velocity
\mathbf{W}	rate of rotation tensor
Δ	computational grid dimensions
$\boldsymbol{\varepsilon}$	infinitesimal strain tensor
κ	smoothing length
λ_S	2 nd Lamé parameter
μ, μ_L	fluid viscosity
μ_S	1 st Lamé parameter/solid shear modulus
ν	Poisson's ratio
ρ	density
$\boldsymbol{\sigma}$	total stress tensor
$\boldsymbol{\tau}$	deviatoric stress tensor
τ	pseudo-time
ψ	level set function

INTRODUCTION

The interaction between liquids and solids is a fundamental requirement for many types of industrial processes. A diverse range of computational methods have successfully been introduced and employed to simulate such processes, based on a variety of formulations. These can be approximately split into two categories – Lagrangian and Eulerian methods. Both methods rely on a spatial and temporal discretisation of the underlying constitutive equations for the system into matrices suitable for numerical solution. In Eulerian methods the

constitutive equations are discretised over a fixed spatial grid, whereas in Lagrangian methods the equations are discretised over a set of points which deforms in some manner with the underlying system. Eulerian methods include finite-volume (FV) and finite element methods, and were pioneered early in the history of computational modelling. Lagrangian methods, such as Smoothed Particle Hydrodynamics (SPH), were introduced later (Monaghan, 1988) and are currently in widespread use.

Typically, simulation of fluid-structure interactions are more challenging for Eulerian than for Lagrangian approaches, as the Eulerian discretisation must conform to boundaries within the system. Such boundaries can be geometric or, in multiphase systems, interfaces between the flow phases. Boundary deformations are especially problematic, as they require the expensive step of regenerating the underlying mesh at each timestep. Recent methods, such as the Immersed Boundary method (Mittal, 2005), have partially overcome these problems, allowing complex geometric objects to be incorporated into simulations with a basic underlying spatial discretisation. Lagrangian methods naturally handle deforming boundaries as the underlying spatial discretisation is effectively updated at each timestep, making such methods extremely effective for simulation of free surfaces and interactions between fluids and complex geometric solids. However, the spatial discretisation inherent in such methods makes specifying advective boundary conditions, such as inflows and outflows, problematic. In contrast, such advective boundary conditions are trivial to implement in Eulerian methods. Lagrangian discretisation also leads to factors such as non-smooth boundary interfaces, making factors such as curvature difficult to determine at phase interfaces.

The level set method (LSM), introduced by Osher and Sethian (1988), is a Eulerian CFD method which allows the modelling of free surface flow without explicit interface tracking. The method builds on the strengths of fixed discretisation Eulerian approaches, allowing the simple implementations of boundary conditions and computational discretisation based on a conservative Navier-Stokes formulation (Sussman et al. 1998). The method is based on the passive advection of a scalar representing a signed distance function, ψ , where the interface in a two-phase mixture is given by the set of zero values of ψ . This signed distance function gives a positive distance from the nearest interface in one phase and a negative distance in the other phase. It can be shown that the distance function in a flow field with velocity field \mathbf{v} is passively advected:

$$\frac{\partial \psi}{\partial t} = -\mathbf{v} \cdot \nabla \psi \quad (1)$$

The characteristic properties of the continuum, such as density ρ and viscosity μ , are defined according to the sign of the distance function:

$$\begin{aligned}\rho &= H(\psi)\rho_1 + (1 - H(\psi))\rho_2 \\ \mu &= H(\psi)\mu_1 + (1 - H(\psi))\mu_2\end{aligned}\quad (2)$$

where ρ_1 is the density of first phase and ρ_2 is the density of second phase. The function H is the Heaviside step function, given by:

$$H(\psi) = \begin{cases} 0 & \psi < 0 \\ \frac{1}{2} & \psi = 0 \\ 1 & \psi > 0 \end{cases}\quad (3)$$

However, due to the discontinuity in Eq. (3), a smoothed Heaviside function is used for practical purposes, where Eq. (3) is smoothed over a characteristic length κ :

$$H(\psi) = \begin{cases} 0 & \psi < -\kappa \\ \frac{1}{2} \left(1 + \frac{\psi}{\kappa} + \frac{1}{\pi} \sin\left(\frac{\pi\psi}{\kappa}\right) \right) & |\psi| \leq \kappa \\ 1 & \psi > \kappa \end{cases}\quad (4)$$

The smoothed density and viscosity defined in Eq. (2) can be used in a standard Navier-Stokes continuum formulation:

$$\rho \left(\frac{\partial \mathbf{v}}{\partial t} + (\mathbf{v} \cdot \nabla) \mathbf{v} \right) = -\nabla p + \nabla \cdot (\mu \mathbf{D}) + \mathbf{f}\quad (5)$$

where p is the pressure, \mathbf{f} are body forces and \mathbf{D} is the rate of strain tensor, $\mathbf{D} = \nabla \mathbf{v} + \nabla \mathbf{v}^T$. The level set method has been used extensively to model free-surface systems such as bubbles, droplets (Sethian, 2003) and charged jets (Hilton and Van der Net, 2009).

MODEL EXTENSION FOR ELASTIC SOLIDS

The starting point for the extended algorithm is the Cauchy momentum equation. This describes the general momentum transport of a continuum material in an Eulerian frame:

$$\rho \left(\frac{\partial \mathbf{v}}{\partial t} + (\mathbf{v} \cdot \nabla) \mathbf{v} \right) = \nabla \cdot \boldsymbol{\sigma} + \mathbf{f}\quad (6)$$

where ρ is the density of the continuum, \mathbf{v} the velocity vector field, $\boldsymbol{\sigma}$ the stress tensor and \mathbf{f} body forces acting on the continuum. The stress tensor is split into an isotropic (pressure) part, p , and a deviatoric part, $\boldsymbol{\tau}$:

$$\rho \left(\frac{\partial \mathbf{v}}{\partial t} + (\mathbf{v} \cdot \nabla) \mathbf{v} \right) = -\nabla p + \nabla \cdot \boldsymbol{\tau} + \mathbf{f}\quad (7)$$

Furthermore, the material in the continuum is assumed to be homogeneous and incompressible, such that:

$$\frac{\partial \rho}{\partial t} + (\mathbf{v} \cdot \nabla) \rho = 0 \rightarrow \nabla \cdot \mathbf{v} = 0\quad (8)$$

In our formulation, we assume that the stress tensor between a solid, $\boldsymbol{\tau}_S$, and liquid, $\boldsymbol{\tau}_L$, can be varied in a similar manner, such that:

$$\boldsymbol{\tau} = H(\psi)\boldsymbol{\tau}_S + (1 - H(\psi))\boldsymbol{\tau}_L\quad (9)$$

We use stress tensors for an hypoelastic solid and a Newtonian fluid, which we show can both be calculated using the known rate of strain tensor \mathbf{D} . For a fluid, the deviatoric stress tensor for a Newtonian fluid is given by:

$$\boldsymbol{\tau}_L = \mu_L \mathbf{D}\quad (10)$$

where the incompressibility condition, $\nabla \cdot \mathbf{v} = 0$, has been used and μ_L is the fluid viscosity. In an isotropic elastic solid, at small strain, $\boldsymbol{\varepsilon}$, the deviatoric stress tensor is given by the linear elastic relation:

$$\boldsymbol{\tau}_S = \mu_S \boldsymbol{\varepsilon} + \lambda_S \text{Tr}(\boldsymbol{\varepsilon})\quad (11)$$

where μ_S and λ_S are the first and second Lamé coefficients, respectively. These play an analogous role in elastic solids to fluid shear viscosity and fluid bulk viscosity. The elastic relation Eq. (11) is only valid for small strain rates and cannot be used to model large deformations. However, Eq. (11) can be generalised to account for large deformations by using a stress rate formulation:

$$\frac{\partial \boldsymbol{\tau}_S}{\partial t} = \mu_S \mathbf{D}\quad (12)$$

The expression given by Eq. (12) is a basic hypoelastic stress rate, which holds for isotropic, homogeneous and incompressible elastic solids (Colak, 2004). In this formulation, μ_S is the shear modulus, $\mu_S = E/2(1 + \nu)$, where E is Young's modulus and ν is Poisson's ratio. As the elastic solid is assumed incompressible, the bulk modulus has no effect and does not enter into the formulation. A closely related model for hyperelastic materials has recently been proposed by Sugiyama et al. (2011), based on a volume of fluid approach.

The time derivative of a Cauchy stress tensor, such as Eq. (12), does *not* hold under rotational transformation. To ensure Eq. (12) is frame indifferent an objective stress rate must be used, such as the Jaumann rate (Benson, 1992):

$$\frac{\partial \widehat{\boldsymbol{\tau}}_S}{\partial t} = \frac{\partial \boldsymbol{\tau}_S}{\partial t} + \boldsymbol{\tau}_S \mathbf{W} - \mathbf{W} \boldsymbol{\tau}_S\quad (13)$$

where \mathbf{W} is the anti-symmetric rate of rotation tensor $\mathbf{W} = \nabla \mathbf{v} - \nabla \mathbf{v}^T$. It should be noted that a number of other such objective stress rates exist, such as Truesdell and the Jaumann rate can give oscillatory solutions (Johnson and Bammann, 1984). However, it is the most straightforward and efficient to implement as it only uses the gradient of the velocity field, which is already calculated for \mathbf{D} , and does not require expensive tensor decompositions. The total deviatoric stress is then given by:

$$\boldsymbol{\tau} = H(\psi) \int_0^t \frac{\partial \widehat{\boldsymbol{\tau}}_S}{\partial t} dt + (1 - H(\psi))\mu_L \mathbf{D}\quad (14)$$

For an interface at $\psi(t) = 0$ with $\mathbf{W} = 0$ the stress tensor is:

$$\boldsymbol{\tau} \sim \mu_S \int_0^t \mathbf{D} dt + \mu_L \mathbf{D} \sim \mu_S \boldsymbol{\varepsilon}(t) + \mu_L \frac{\partial \boldsymbol{\varepsilon}}{\partial t}\quad (15)$$

Hence the interface between the solid and liquid phase acts as a viscoelastic Voigt material.

NUMERICAL METHODOLOGY

The constitutive relations, Eqs. (5, 14) are discretised onto a semi-staggered grid with pressure, stress tensors, the level set function and porosity defined at the cell centres and forces and velocities defined at the cell corners. The staggering of the grid cells in this manner reduces the formation of 'checkerboard' pressure oscillations. Advection terms, including the level set advection equation, are updated using a conservative finite volume MUSCL scheme (Nessyahu and Tadmor, 1990) with a MinMod limiter. Diffusion terms are discretised using

second order stencils. The system is solved using an incremental pressure correction method, where the Poisson terms are solved using a pre-conditioned conjugate gradient method, with a SSOR pre-conditioner.

The stress tensor is calculated in a series of stages. First, the velocity gradient, $\nabla \mathbf{v}$, at the centre of each cell is evaluated using the values from the edges of the cell. Next, these values of $\nabla \mathbf{v}$ are used to calculate the rate of strain tensor $\mathbf{D} = \nabla \mathbf{v} + \nabla \mathbf{v}^T$ and the rate of rotation tensor $\mathbf{W} = \nabla \mathbf{v} - \nabla \mathbf{v}^T$. Eq. (13) is then evaluated using a second-order accurate half-step temporal discretisation (Benson, 1992):

$$\begin{aligned} \boldsymbol{\tau}_S^{n+\frac{1}{2}} &= \boldsymbol{\tau}_S^n + \boldsymbol{\tau}_S^n \mathbf{W} - \mathbf{W} \boldsymbol{\tau}_S^n \\ \boldsymbol{\tau}_S^* &= \boldsymbol{\tau}_S^{n+\frac{1}{2}} + \Delta t \mu_S \mathbf{D}^n \end{aligned} \quad (16)$$

$$\boldsymbol{\tau}_S^{n+1} = \boldsymbol{\tau}_S^* + \boldsymbol{\tau}_S^* \mathbf{W} - \mathbf{W} \boldsymbol{\tau}_S^*$$

After the solid stress tensor is calculated, the total stress tensor, Eq. (9) is evaluated and used in the generalised transport equation, Eq. (7). The steps in Eq. (16) represent the numerical integration of the temporal term in Eq. (14).

As the level set is advected by the velocity flow field, the signed distance property can become distorted. This can cause spurious gradients to occur in the level set field, resulting in errors to the interface. For this reason, the level set must be re-initialised to conform to a signed distance function. There is a considerable amount of literature devoted to this particular step in the algorithm, as it involves the approximate solution of the Eikonal equation, and is therefore an expensive operation to perform. Furthermore, the act of re-initialising the level set can cause erroneous mass loss near sharp edges on the interface. Such mass loss must be accounted for in the re-initialisation scheme. In this implementation we use the method originally developed by Sussman et al. (1998). The Eikonal equation converges to the distance function from the interface given by the level set at the start of the re-initialisation, ψ_0 :

$$\begin{aligned} \frac{\partial \psi}{\partial \tau} &= \text{sign}(\psi_0)(1 - |\nabla \psi|) \\ \psi(\tau = 0) &= \psi_0 \end{aligned} \quad (17)$$

This expression can be evaluated to convergence in the pseudo-time τ . However, to correct for mass loss during this procedure this expression is evaluated with an additional conservation condition within each cell Ω :

$$\frac{\partial}{\partial \tau} \int_{\Omega} H(\psi) = 0 \quad (18)$$

This results in the following augmented Eikonal equation:

$$\begin{aligned} \frac{\partial \psi}{\partial \tau} &= \text{sign}(\psi_0)(1 - |\nabla \psi|) + \lambda f(\psi) \\ \psi(\tau = 0) &= \psi_0 \end{aligned} \quad (19)$$

where $f(\psi)$ is chosen by Sussman to be:

$$f(\psi) = \frac{\partial H(\psi)}{\partial \tau} |\nabla \psi| \quad (20)$$

and λ is calculated to be:

$$\lambda = \frac{-\int_{\Omega} \frac{\partial H(\psi)}{\partial \tau} (\text{sign}(\psi_0)(1 - |\nabla \psi|))}{\int_{\Omega} \frac{\partial H(\psi)}{\partial \tau} f(\psi)} \quad (21)$$

The integrals in Eq. (21) are evaluated using a 27-point stencil over the neighbouring cells.

APPLICATIONS

The method was applied to two test case scenarios. The first was an elastic block falling in a fluid and impacting on a fixed, solid, horizontal cylinder. The second case was fluid flow through a porous bed, where the porous material was a flexible elastic solid.

Free falling elastic block

As a first qualitative test case an elastic block freely falling under gravity and impacting on a fixed object was modelled. This case was chosen to test the elastic response of the solid material, the interaction with fluid in the domain as well as to assess the behaviour of the Jaumann rate under large topological rotations. The computational domain was a square box, 10 cm on each side, containing a flat cuboidal elastic solid measuring 6 cm \times 6 cm \times 2 cm. For ease of set-up this block was modelled using the implicit surface equation for a superquadric:

$$\psi(x, y, z) = x^8 + (4y)^8 + z^8 - 1 \quad (22)$$

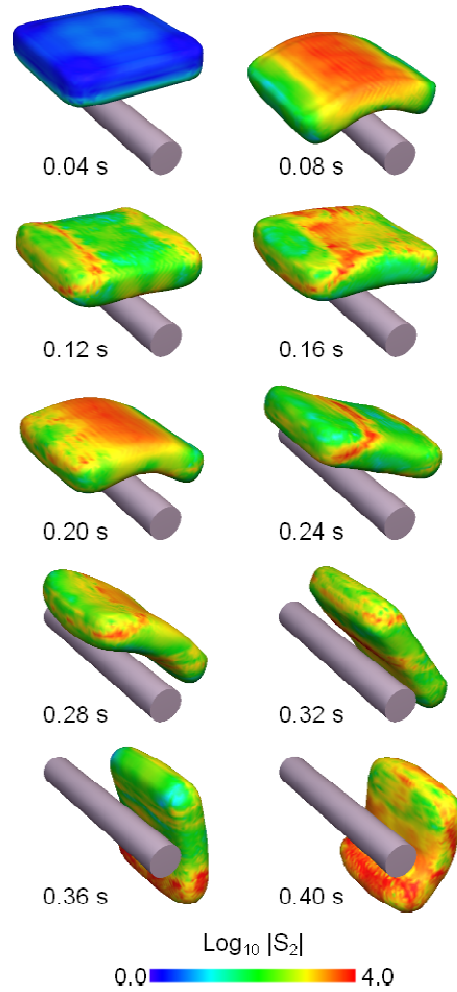


Figure 1 - Time evolution of a free-falling square elastic block with $\mu_S = 1000$. The surface of the elastic solid is shaded by the logarithm of the second invariant of the stress tensor.

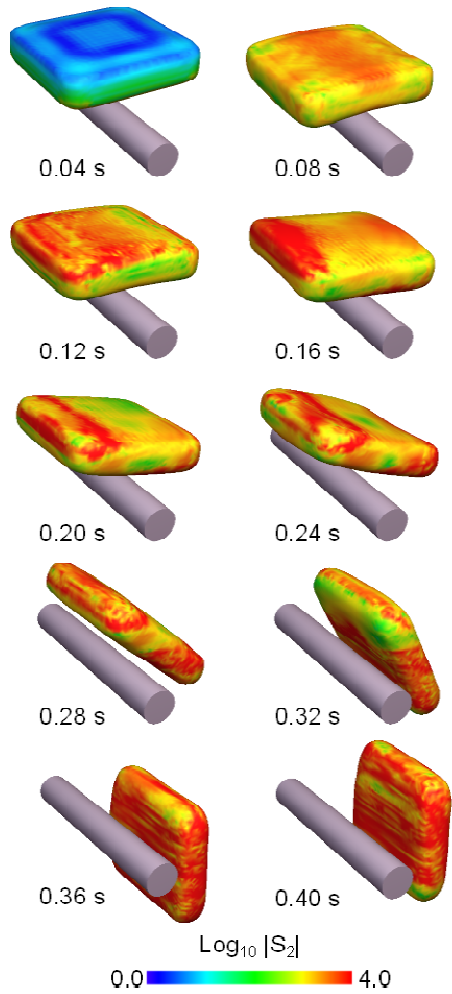


Figure 2 - Time evolution of a free-falling square elastic block with $\mu_S = 5000$. The surface of the elastic solid is shaded by the logarithm of the second invariant of the stress tensor.

After initialisation with Eq. (22) the exact distance function was found using the Fast Marching Algorithm (Sethian, 1998). The density of the block was set to 100 kg/m^3 , and the density of the surrounding fluid was set to approximately that of air, 1 kg/m^3 . The block fell freely until it impacted with a horizontal solid cylinder. The solid cylinder was implemented by setting the updated velocity for all cells within the cylinder to zero at each time step. Such an approach is not restricted to fixed objects, however, and methods such as the Immersed Boundary method (Mittal, 2005) can be used to prescribe any velocity within the domain. The grid dimensions were $75 \times 75 \times 75$ cells, and the simulation was run for 0.5 s at a timestep of 10^{-5} s .

The response of the elastic material was evaluated for three different values of μ_S : 1000, 2000 and 5000. Figures 1 and 2 show the results for $\mu_S = 1000$ and $\mu_S = 5000$, respectively. The value of $\mu_S = 2000$ has been omitted at it essentially shows intermediate behaviour. The surface of the elastic solid is shown in the figures, shaded by the magnitude of the logarithm of the second stress invariant, $S_2 = \tau_{00}\tau_{11} + \tau_{11}\tau_{22} + \tau_{22}\tau_{00} + \tau_{01}^2 + \tau_{12}^2 + \tau_{20}^2$.

In all simulations the block fell, impacted the cylinder ($t \sim 0.06 \text{ s}$), deformed and rebounded, hitting the cylinder again ($t \sim 0.2 \text{ s}$) before sliding to the side of the cylinder

and impacting the solid base ($t \sim 0.36 \text{ s}$). A non-uniform stress distribution over the object before impact ($t \sim 0.04 \text{ s}$) can be seen in Figs. 1 and 2, with a high stress component around the edges on the underside of the object. This was caused by pressure gradient over the object from the surrounding air, showing that the method correctly handles stress transmission over the fluid-solid boundary. After impact, deformation of the material was found to be lower at higher shear modulus, as shown by comparing Figs.1 and 2. This can be most clearly seen by comparing the degree of bending just after the initial impact ($t \sim 0.08 \text{ s}$) between the two simulations. Stress waves also propagated through the object, initiating at the centre on impact and rebounding from the sides of the object. Such waves can be seen at $t = 0.12$ and $t = 0.24$ in the simulation with $\mu_S = 1000$.

The numerical method accurately modelled the dynamics of the object. After rotation through 90° around the cylinder, the object was essentially unchanged from the initial configuration, showing that the level set method correctly captured the geometric transformations of the object. Furthermore, propagation of stress waves were unaffected as the object rotated, showing that Jaumann rate, Eq. (13), updated the stress tensor correctly in an objective manner using the half step method given by Eq. (16).

Flexible porous bed

As a second, quantitative, test of the method we simulated gas flowing through a porous bed, composed of a packing of bonded elastic spheres. Flow within porous media is strongly dominated by the drag from internal boundaries, and this case was chosen to investigate the effect of the viscoelastic boundaries, Eq. (15), in the methodology.

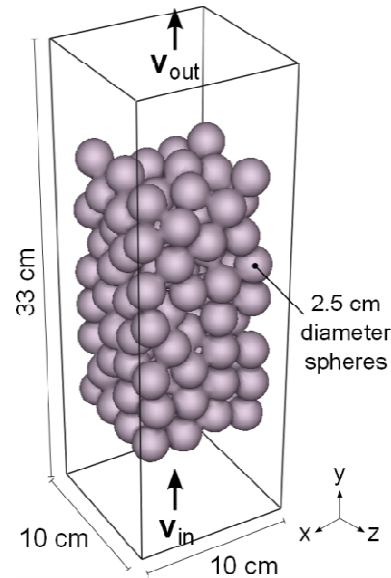


Figure 3 – Set-up for gas flow through a flexible porous medium.

A spherical packing was prepared using a discrete element simulation and used as the initial conditions for the level set. The computational domain was a rectangular duct with dimensions $11 \text{ cm} \times 33 \text{ cm} \times 11 \text{ cm}$, filled with bonded spheres of diameter 2.5 cm . The computational grid had dimensions $50 \times 150 \times 50$, giving a grid spacing $\Delta = 2.2 \times 10^{-3} \text{ m}$. The smoothing length κ was

chosen as 2 grid cells, $\kappa = 2\Delta$. The initial set-up is shown in Fig. 3.

Gas was injected into the system at the base and drawn from the top at an equal mass flow rate. In order to fix the porous block in place zero-velocity boundary conditions are applied over five grid cells (1.1 cm) from the side wall boundaries. A set of simulations were carried out with the inflow velocity fixed at 0.1 m/s and different shear moduli, μ_s , of 100, 250, 500, 750 and 1000. The density of the elastic solid was 10 kg/m³, and the density of the gas was 1 kg/m³. The gas viscosity was set to 1×10^{-5} Pa s.

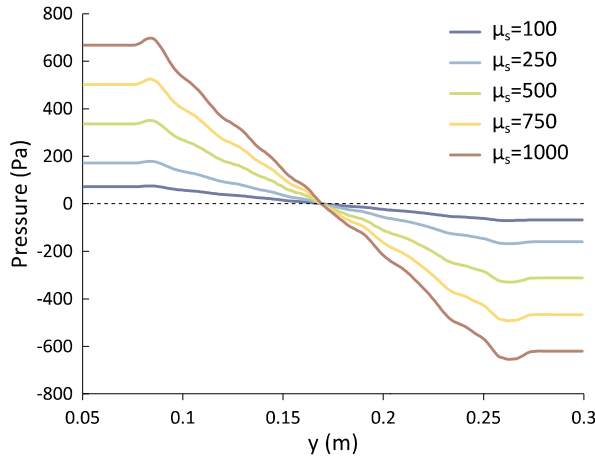


Figure 4 - Pressure along vertical midline for fluid flow through a flexible porous medium, with shear moduli, μ_s , of 100, 250, 500, 750 and 1000.

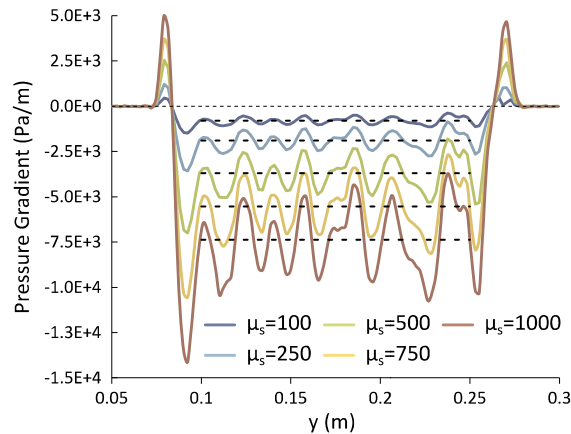


Figure 5 - Pressure gradient along vertical midline for fluid flow through a flexible porous medium, with shear moduli, μ_s , of 100, 250, 500, 750 and 1000. Average pressure gradients from 0.1 to 0.25 m are shown as dashed lines.

The pressure drop over the porous bed is shown in Fig.4 for all shear moduli considered at $t = 1$ s. The pressure was measured along the vertical midline along y at $x = 5$ cm, $z = 5$ cm. The pressure dropped approximately linearly over the bed, with the gradient proportional to the shear modulus of the bed material. The pressure gradient is shown in Fig. 5, along with the average pressure gradient within the interior of the bed. The average pressure gradient is shown as dashed lines, where the interior was defined as $y = 0.1$ m to $y = 0.25$ m. Although there were considerable gradient fluctuations

within the bed, the average pressure gradient was found to scale in an exact linear manner with the shear modulus, as shown in Fig. 6. The pressure distribution over the surface of the bed is also shown in Fig. 7 at $t = 1$ s for $\mu_s = 100$ and $\mu_s = 1000$. The pressure distribution is very similar in both cases, approximately linear in the vertical direction, differing only by the magnitude of the gradient.

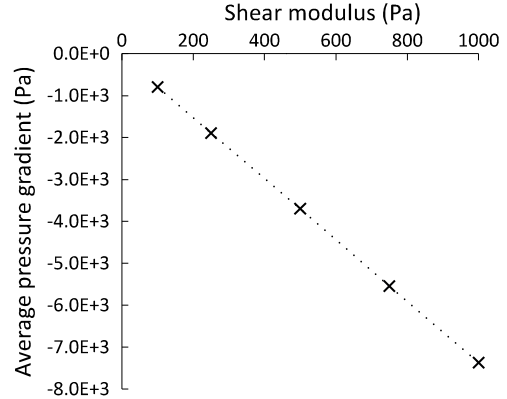


Figure 6 - Average pressure gradient over the bed at $t = 1$ s against bed shear modulus.

The pressure gradient in the simulations was found to be much greater than for gas flow through a bed of regular, non-elastic, particles. The Reynolds number for this system is ~ 250 , so the pressure gradient for idealised gas flow through a bed of spherical particles can be determined using the Ergun equation (Ergun, 1952):

$$\nabla p = \left(\frac{1 - \varepsilon}{\varepsilon^3} \right) \frac{\rho |\mathbf{v}|^2}{d} \left(\frac{150(1 - \varepsilon)\mu}{d|\mathbf{v}|\rho} + 1.75 \right) \quad (23)$$

where ε is the voidage fraction, d the sphere diameter, ρ the gas density and μ the gas viscosity. For the parameters used in this set up, the Ergun relation gives a pressure gradient over the bed of 11 Pa/m, in comparison to $O(1000)$ Pa/m in the simulations. A linear fit to the pressure gradient against shear modulus relation in Fig. 6 has a non-zero intercept at $O(10)$ Pa/m, so ordinary porous flow behaviour returns in the limit $\mu_s \rightarrow 0$. The excess pressure gradient therefore arises from the elastic component of the model.

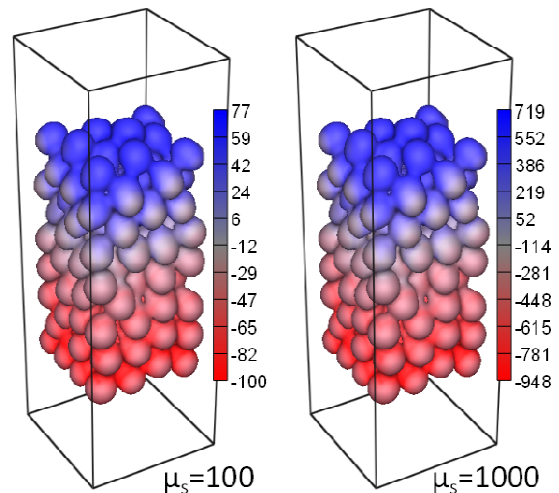


Figure 7 - Pressure distribution over elastic porous bed with shear moduli, μ_s , of 100 (left) and 1000 (right) at $t = 1$ s.

Inspection of the simulations showed that this excess pressure gradient was not caused by elastic expansion over the bed, as the degree of deformation within the porous bed was found to be very similar over the range of shear moduli used. A close-up view of the top part of the bed is shown in Fig. 8 for $\mu_s = 100$ and $\mu_s = 1000$ at the start of the simulation, $t = 0.5$ s and $t = 1.0$ s. The dashed circles in these figures indicate the initial position of one of the spheres within the bed for comparison. The bed deformed approximately 10 mm in the vertical direction, with almost negligible difference between both cases.

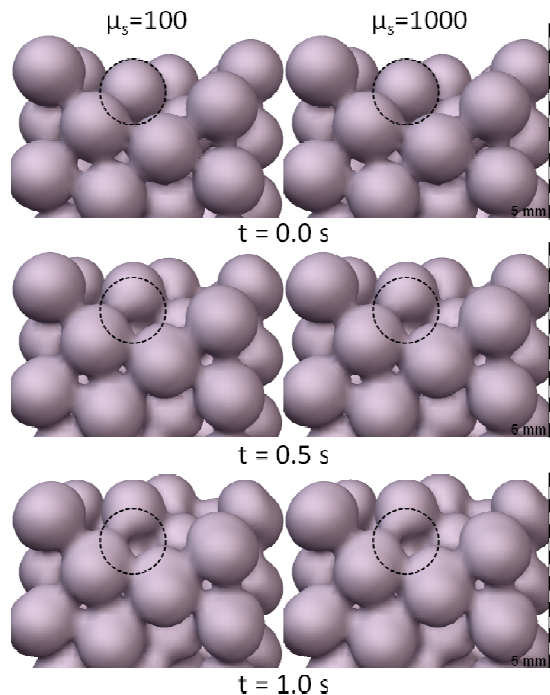


Figure 8 – Comparison of bed deformation for $\mu_s = 100$ and $\mu_s = 1000$ at $t = 0.0, 0.5, 1$ s.

The boundary conditions, Eq. (15), are therefore responsible for this excess pressure, greatly increasing the relative gas-solid drag through viscoelastic interaction. This effect scales linearly with shear modulus, as shown in Fig. 6. The flow of viscoelastic fluid through porous media has received attention both experimentally (Slattery, 1967) and computationally (Ariel, 1993). However, to our knowledge such a system with flexible, viscoelastic boundaries has not previously been modelled and such a linear drag relation between pressure gradient with shear modulus has not previously been established. Further investigation of this system is planned to fully understand the physical nature of this drag relation.

CONCLUSION

The level set method can be extended to model the interaction between a Newtonian fluid and an elastic solid. This can be implemented by varying the stress tensor over the computational domain depending on the sign of the level set function. The stress tensor depends only on the local strain rate within the fluid, but includes a history-dependant part within the solid. Use of a smoothing function causes viscoelastic Voigt behaviour of the material over the boundary between the interfaces.

Two test cases were simulated using the model. Elastic falling bodies showed good qualitative behaviour

in interaction with solid boundaries, as well as in response to change in shear modulus. It was also found that boundary-dominated flow through a porous bed showed a linear relation between pressure gradient and shear modulus. These basic cases highlight the capability of the model to fully resolve the coupled dynamics of elastic solids with a fluid flow field, showing the potential of the model for possible application to a wide range of industrial applications.

REFERENCES

- ARIEL, P. D., (1993), "Flow of Viscoelastic fluids through a porous channel – I", *I. J. Num. Meth. Fluids*, **17**, 605-633.
- BENSON, D. J., (1992), "Computational methods in Lagrangian and Eulerian hydrocodes", *Computer Methods in Applied Mechanics and Engineering*, **99**, 235 – 394.
- COLAK, O. U., (2004), "Modeling of large simple shear using a viscoplastic overstress model and classical plasticity model with different objective stress rates", *Acta Mechanica*, **167**, 171-187
- ERGUN, S., (1952), "Fluid flow through packed columns", *Chem. Eng. Prog.*, **48**, 89-94
- HILTON, J. E., VAN DER NET, A., (2009), "Dynamics of charged hemispherical soap bubbles", *EPL*, **86**, 24003
- JOHNSON, G. C. and BAMMANN, D. J., (1984), "A discussion of stress rates in finite deformation problems", *Int. J. Solid Structures*, **20**, 725-737.
- MITTAL, R., (2005), "Immersed boundary methods", *Annual Review of Fluid Mechanics*, **37**, 239-261.
- MONAGHAN, J.J. (1988), "An introduction to SPH", *Computer Physics Communications*, **48**, 88-96.
- NESSYAHU, H. and TADMOR, E., (1990), "Non-oscillatory central differencing for hyperbolic conservation laws", *J. Comp. Phys.*, **87**, 408-463.
- OSHER, S. and SETHIAN, J. A., (1988), "Fronts propagating with curvature-dependent speed: Algorithms based on Hamilton–Jacobi formulations", *J. Comp. Phys.* **79**, 12-49.
- SETHIAN, J. A., (1998), "Fast Marching Methods", *SIAM Review*, **41**, 199-235.
- SETHIAN, J. A., (2003), "Level Set Methods for Fluid Interfaces", *Annual Review of Fluid Mechanics*, **35**, 341-372.
- SLATTERY, J. C., (1967), "Flow of Viscoelastic Fluids Through Porous Media", *AIChE J.*, **13**, 1066-1071
- SUGIYAMA, K., II, S., TAKEUCHI, S., TAKAGI, S., MATSUMOTO, Y., (2011), "A full Eulerian finite difference approach for solving fluid-structure coupling problems", *Journal of Computational Physics*, **230**, 596-627
- SUSSMAN, M., FATEMI, E., SMEREKA, P. and OSHER, S. (1998), "An improved level set method for incompressible two-phase flows", *Computers & Fluids*, **27**, 663-680.